PAPER

Construction of unique $NiCo_2O_4$ nanowire@$CoMoO_4$ nanoplate core/shell arrays on Ni foam for high areal capacitance supercapacitors†

Daoping Cai, Bin Liu, Dandan Wang, Lingling Wang, Yuan Liu, Han Li, Yanrong Wang, Qiuhong Li and Taihong Wang*

In this work, we present a facile two-step hydrothermal method with a successive annealing treatment to integrate two ternary metal oxides ($NiCo_2O_4$ and $CoMoO_4$) into unique core/shell nanowire arrays (NWAs) on Ni foam as advanced binder-free electrodes for the first time. In addition, a possible growth mechanism for the growth of $CoMoO_4$ nanoplates (NPs) on $NiCo_2O_4$ nanowires (NWs) is put forward based on the time-dependent experiments. When investigated as binder-free electrodes for supercapacitors (SCs), such unique $NiCo_2O_4$@$CoMoO_4$ core/shell hybrid electrodes exhibit ultrahigh areal capacitances, which are several times larger than the pristine $NiCo_2O_4$ electrode. The remarkable electrochemical performance is attributed to the rational combination of two electroactive materials and the reasonable array configuration.

1. Introduction

With the rapid depletion of fossil fuels and increasingly worsened environmental pollution, energy storage is becoming one of the great challenges in the twenty-first century.[1,2] Compared with other energy storage systems such as batteries and fuel cells, SCs are superior in the areas of high power density, fast charge–discharge process, long cycle life, low maintenance cost, and safety.[3–5] Based on the charge storage mechanism, SCs are generally classified into two types: electric double layer capacitors (EDLCs) and pseudocapacitors.[6,7] In recent years, scientists have made a lot of progress in the theoretical and practical research and development of SCs.[8–12] Undoubtedly, recent progress in supercapacitor technology benefits much from the nanostructured electrodes instead of traditional ones. Nanostructured materials have been considered as promising candidates for highly efficient electrodes of energy conversion/ storage devices because of their high surface area, short electron and ion transport pathways.[13,14]

Currently, one of the great progresses is directly growing electrode materials on a current collector, which attracts more and more attention. As we know, traditional supercapacitor electrodes are fabricated by mixing the electroactive materials, binders, and additives with an organic solvent into a slurry and then pressed onto the current collector.[15] In such binder-

enriched electrodes, a large portion of the electroactive surface of the electrode materials is blocked from contact with the electrolyte to participate in the Faradaic reactions. Furthermore, the electrical conductivity of the electrode materials seriously decreases owing to the existence of the polymer binder.[16–18] Compared with the binder-enriched electrodes, directly growing ordered nanostructure arrays on the current collector not only simplifies the electrode processing, but also offers remarkable advantages such as easy diffusion of electrolyte, better electrical contact with substrates, sufficient electrochemical reaction of individual nanostructures and enhanced electrode–electrolyte contact area.[19–21] Till now, vertically well-aligned arrays of 1D nanostructures (nanowire, nanotube, nanowall, nanosheet, etc.) have been synthesized as advanced electrodes for high performance supercapacitor applications. More recently, tremendous efforts have been devoted to the rational synthesis of advanced core/shell heterostructures, which represent a promising approach to boost the electrochemical performance of single components. By combining unique properties of individual constituents, improved performance has been realized in such electrodes.[22–26] In most cases, such hierarchical core/shell heterostructures consist of highly conductive materials as the core and transition metal oxides or hydroxides as the shell. Various core/shell heterostructures have been synthesized and shown superior electrochemical performance owing to their synergistic effects. For example, Yu et al. reported novel hierarchical $NiCo_2O_4$@MnO_2 core/shell heterostructured NWAs, which delivered higher areal capacitance of 3.31 F cm^{-2} than $NiCo_2O_4$ NWAs (2.01 F cm^{-2}) at 2 mA cm^{-2}.[27] Xia et al. reported Co_3O_4@NiO core/shell NWAs for SCs

Pen–Tung Sah Institute of Micro–Nano Science and Technology, Xiamen University, Xiamen 361000, P.R. China. E-mail: thwang@xmu.edu.cn

with an improved capacitance (1.35 F cm^{-2} at 1.67 A g^{-1}) which was 2 and 5 times larger than the Co_3O_4 NWAs (0.68 F cm^{-2}) and NiO nanoflake arrays (0.25 F cm^{-2}), respectively.[24]

Despite of these progresses, however, it still remains a big challenge to develop cost-effective and simple methods for the fabrication of core/shell NWAs with well defined morphologies and tunable functions. In this work, we present a facile two-step hydrothermal method with a successive annealing treatment to integrate two ternary metal oxides ($NiCo_2O_4$ and $CoMoO_4$) into unique core/shell NWAs on Ni foam as advanced binder-free electrodes for the first time. By controlling the reaction times, a series of unique $NiCo_2O_4@CoMoO_4$ nanostructures have been synthesized and investigated as binder-free electrodes for SCs. This electrode design has many apparent advantages such as: (1) both the core and shell materials are promising pseudocapacitive materials for SCs, making a contribution to the total capacitance;[24,26,27] (2) the highly porous $NiCo_2O_4$ NWs with good electrical conductivity act as the backbone and electron "superhighway" for charge storage and delivery;[28] (3) the high mass loading of thin $CoMoO_4$ NPs onto the $NiCo_2O_4$ NWs greatly enhances the surface area, providing more electroactive sites for Faradaic reactions;[23] (4) the open space between each core/shell nanowire allows for easy diffusion of the electrolyte into the inner region of the electrode, resulting in a high utilization of the electrode materials;[29,30] (5) furthermore, directly growing ordered nanostructure arrays on current collector ensures good mechanical adhesion and electrical connection to the current collector, avoiding the use of polymer binder and conductive additives, improving the utilization of the electrode material, and thus resulting in high capacitance even under high current densities.[19–21] Benefiting from these advantages, such unique $NiCo_2O_4@CoMoO_4$ core/shell hybrid electrodes exhibit remarkable electrochemical performance, and hold great promise for high-performance energy storage applications.

2. Experimental

2.1. Materials synthesis

All the reagents used in the experiments were of analytical grade and used without further purification.

Synthesis of $NiCo_2O_4$ NWAs: Prior to the synthesis, the Ni foam (2 × 1 × 0.1 cm) was cleaned by sonication in acetone, ethanol, and deionized (DI) water in sequence for 10 min each. The $NiCo_2O_4$ NWs growing on Ni foam was realized by a modified technique according to the literature.[31] In a typical synthesis, 1.45 g $Co(NO_3)_2 \cdot 6H_2O$, 0.59 g $NiCl_2 \cdot 6H_2O$ and 0.45 g urea were dissolved in 35 mL deionized (DI) water under constant magnetic stirring to form a clear pink solution. The solution was transferred to a 50 mL Teflon-lined stainless steel autoclave with a piece of pretreated Ni foam immersed into the reaction solution. The autoclave was sealed and maintained at 120 °C for 6 h, and then cooled down to room temperature. The array sample was collected and rinsed with distilled water several times, followed by annealing at 400 °C in air for 3 h.

Synthesis of $NiCo_2O_4@CoMoO_4$ hybrid NWAs:[30] In a typical synthesis, 2 mmol $Co(NO_3)_2 \cdot 6H_2O$ and 2 mmol $Na_2MoO_4 \cdot 7H_2O$

were dissolved into 30.0 mL deionized (DI) water. The mixture was kept under an intense ultrasonic treatment for a few minutes in order to form a light purple solution and then transferred to a 50 mL Teflon-lined stainless steel autoclave. Afterwards, a piece of Ni foam with $NiCo_2O_4$ NWAs grown was immersed into the reaction solution. In order to investigate the growth process, the autoclave was sealed and maintained at 160 °C for different times. After the reaction was over, the array samples were taken out and rinsed with distilled water and alcohol several times, followed by annealing at 400 °C in air for 2 h.

2.2. Materials characterization

The powder X-ray diffraction (XRD) patterns were recorded on a Panalytical X-pert diffractometer with Cu Kα irradiation. The morphology and crystal structure were observed by scanning electron microscopy (SEM, Hitachi S4800) and high-resolution transmission electron microscopy (HRTEM, JEM-2100) with an acceleration voltage of 200 kV.

2.3. Electrochemical measurements

The electrochemical measurements were carried out in a three-electrode electrochemical cell containing 2 M KOH aqueous solution as the electrolyte. The $NiCo_2O_4$ NWAs and $NiCo_2O_4@CoMoO_4$ hybrid NWAs were directly used as the working electrodes. The area of the working electrodes immersed into the electrolyte was controlled to be about 1 cm^2. The electrochemical measurements were conducted with a CHI660E electrochemical workstation. A standard calomel electrode (SCE) was used as the reference electrode and a Pt foil as the counter electrode, and all the experiments were done at ambient temperature. EIS measurements were performed by applying an AC voltage with 5 mV amplitude in a frequency range from 0.01 Hz to 100 kHz. The capacitance (C), energy density (E) and power density (P) were calculated according to the following equations:[10,13]

$$C = \frac{It}{SV} \text{ or } C = \frac{It}{mV} \tag{1}$$

$$E = \frac{1}{2}CV^2 \tag{2}$$

$$P = \frac{E}{t} \tag{3}$$

where I was the constant discharge current (A), t was discharge time (s), V was the potential window (V), S was the geometrical area (cm^2) of the electrode and m was the mass (g) of the active material on the electrode.

3. Results and discussion

The morphologies of the $NiCo_2O_4$ NWs and $NiCo_2O_4@CoMoO_4$ (12 h) core/shell NWs on nickel foam are shown in Fig. 1. After hydrothermal growth, the whole surface of the nickel foam is uniformly covered by the $NiCo_2O_4$ NWs (Fig. 1A). The $NiCo_2O_4$ NWs have an average diameter of 200 nm and length up to
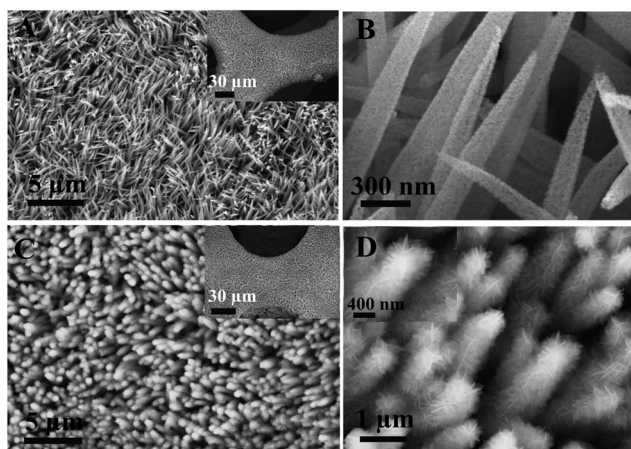
Fig. 1 Typical SEM images of the NiCo$_2$O$_4$ NWAs on Ni foam at (A) low and (B) high magnifications; typical SEM images of the NiCo$_2$O$_4$@CoMoO$_4$ (12 h) core/shell NWAs on Ni foam at (C) low and (D) high magnifications.

around 8 μm. The magnified image reveals they are highly porous, and are composed of numerous interconnected nano-grains (Fig. 1B). After a 12 h hydrothermal reaction, the surface of the NiCo$_2$O$_4$ NWs becomes rough, fully covered by the CoMoO$_4$ NPs forming a core/shell nanostructure. The NiCo$_2$O$_4$ nanowires can provide a vast quantity of sites for the growing of CoMoO$_4$ nanoplates, resulting in a high mass loading of the CoMoO$_4$ nanoplates. It is worth noting that the uniformity of the nanostructure is still well retained. The obtained NiCo$_2$O$_4$@CoMoO$_4$ core/shell NWAs are well aligned on the substrate on a large scale (Fig. 1C). The CoMoO$_4$ NPs are very thin, which is observed from the magnified image (Fig. 1D). This electrode design will greatly increase the surface area, providing more electroactive sites for Faradaic reactions and leading to high area capacitance. In such a unique hierarchical structure, the open space between the core/shell NWs in the array can be efficiently utilized, ensuring an easy diffusion of the electrolyte ions to the surface of the active material.[29] The composition of the obtained NiCo$_2$O$_4$ and NiCo$_2$O$_4$@CoMoO$_4$ (12 h) hybrid NWs were studied by XRD and the corresponding XRD patterns are shown in Fig. 2. The peaks marked with "*" are typical peaks from the Ni foam substrate. The four major
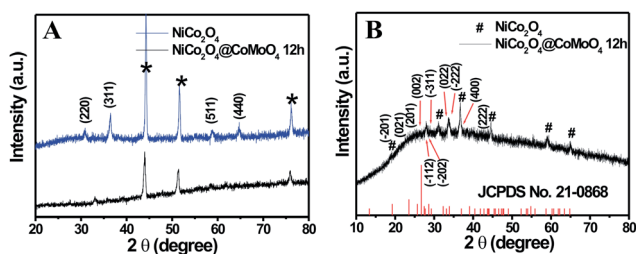
peaks in the pattern of NiCo$_2$O$_4$ can be well indexed to the (220), (311), (511) and (440) planes of the cubic NiCo$_2$O$_4$ phase (JCPDS card no. 20-0781).[13] After the hydrothermal growth of the CoMoO$_4$ NPs, the peaks from the NiCo$_2$O$_4$ and Ni foam become weak. In order to preclude the strong impact of the Ni foam substrate on the XRD peak signals, the NiCo$_2$O$_4$@CoMoO$_4$ (12 h) core/shell composite is scratched from Ni foam for further identification. As shown in Fig. 2B, the peaks marked with "#" are from NiCo$_2$O$_4$, and the other new diffraction peaks can be indexed to monoclinic CoMoO$_4$ phase (JCPDS card no. 21-0868), which is consistent with the literature results.[32,33]

The nanostructures of the NiCo$_2$O$_4$ and NiCo$_2$O$_4$@CoMoO$_4$ (12 h) core/shell NWs were further investigated using TEM. The typical TEM image of an individual NiCo$_2$O$_4$ nanowire is shown in Fig. 3A, providing further information of the highly porous structure, which is consistent with the SEM observation. The NiCo$_2$O$_4$ nanowire is composed of numerous interconnected nanoparticles with sizes of 20–40 nm (Fig. 3B). From the HRTEM image (the inset in Fig. 3B) taken from the marked area, the spacing of the lattice fringes is calculated to be 0.29 nm, which can be indexed as the (220) plane of cubic NiCo$_2$O$_4$ phase, which is in accordance with the XRD data. The typical TEM image of an individual NiCo$_2$O$_4$@CoMoO$_4$ core/shell nanowire is shown in Fig. 3C. Although the NiCo$_2$O$_4$ nanowire is completely covered by CoMoO$_4$ NPs, the core/shell nano-structure can still be distinguished from the magnified TEM image (Fig. 3D). The exact thickness of the CoMoO$_4$ NPs is about 22 nm as revealed by the magnified TEM image. The HRTEM image taken from the shell are also exhibited in Fig. 3D (the inset). The lattice fringes show an interplanar spacing of about 0.21 nm, corresponding to the (222) plane of the monoclinic CoMoO$_4$ phase. In addition, the energy-dispersive X-ray spec-trometry (EDS) analysis also confirms the NiCo$_2$O$_4$@CoMoO$_4$ core/shell structure. As shown in Fig. 3E, only the signals of Ni and Co are found in the core region, and the signals of Mo are obtained from the shell region, further confirming the NiCo$_2$O$_4$@CoMoO$_4$ core/shell nanostructure. Note that the Cu signal is from the carbon-supported Cu grid. In addition, mapping results indicate that Ni, Mo and O elements are homogeneously and uniformly distributed throughout the sample (Fig. S1†).

To investigate the growth process of the CoMoO$_4$ NPs on NiCo$_2$O$_4$ NWs grown on Ni foam, a series of experiments with different hydrothermal reaction times are performed. Fig. 4A exhibits a schematic illustration of the possible growth mechanism of the CoMoO$_4$ NPs on NiCo$_2$O$_4$ NWs. The SEM images of the products obtained at different reaction times are shown in Fig. 4B–F. The mixing of MoO$_4^{2-}$ and Co^{2+} aqueous solutions could immediately lead to the formation of CoMoO$_4 \cdot n$H$_2$O crystalline nuclei.[32] Before reaction, there are no nanoparticles on the surface of the NiCo$_2$O$_4$ NWs. After being put into the above solution, the nanoparticles start to attach to the surface of the core. At the early stage (4 h), some parts of the core are not covered by the nanoparticles. When the reaction time is prolonged to 8 h, the surface of the core is almost covered by the small CoMoO$_4$ NPs. On further increase of the reaction time, these small CoMoO$_4$ NPs grow up to form a larger

Fig. 2 Typical XRD patterns of (A) the NiCo$_2$O$_4$ NWAs and NiCo$_2$O$_4$@CoMoO$_4$ (12 h) core/shell NWAs on Ni foam; (B) XRD pattern of the NiCo$_2$O$_4$@CoMoO$_4$ (12 h) core/shell composite scratched from Ni foam.
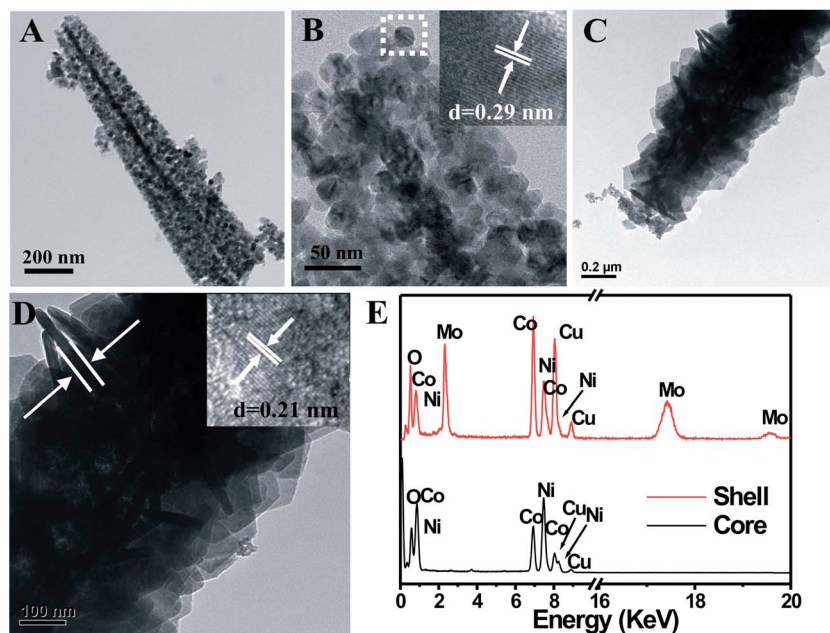
Fig. 3 (A) Typical TEM image and (B) high-magnification TEM image of the $NiCo_2O_4$ nanowire and inset the HRTEM image; (C) typical TEM image and (D) high-magnification TEM image of the $NiCo_2O_4@CoMoO_4$ (12 h) core/shell nanowire and inset the HRTEM image taken from the shell region; (E) EDS analysis of the $NiCo_2O_4@CoMoO_4$ (12 h) core/shell nanowire.

size with greater thickness, leading to less space between each core/shell nanowire.

The electrochemical performance of the $NiCo_2O_4$ NWAs and $NiCo_2O_4@CoMoO_4$ hybrid NWAs were evaluated as binder-free electrodes for SCs. The electrochemical tests were carried out in a three-electrode configuration with a Pt plate counter electrode and a calomel reference electrode in 2 M KOH aqueous electrolyte. Fig. 5A shows the cyclic voltammogram (CV) curves of the pristine $NiCo_2O_4$ (denoted as 0 h) and $NiCo_2O_4@CoMoO_4$ (8, 12, and 18 h) hybrid electrodes recorded at a scan rate of 5 mV s^{-1}. The shape of the CV curves clearly indicates the existence of the Faradaic process, which is mainly attributed to the Faradaic redox reactions related to M–O/M–O–OH, where M

refers to Ni or Co.[13,32] Compared with the pristine $NiCo_2O_4$ electrode, the cathodic peaks of the $NiCo_2O_4@CoMoO_4$ hybrid electrodes shift to lower potential, which is due to the polarization effect of the electrodes.[34] The $CoMoO_4$ NPs of the 18 h sample are larger and the neighbouring $NiCo_2O_4@CoMoO_4$ core/shell nanowires can partially connect to each other (Fig. 4F). This connection can provide a lateral pathway for electron transport, resulting in a smaller polarization effect of the electrode than the 12 h sample. Obviously, the enclosed area of the hybrid electrodes are much larger than that of pristine $NiCo_2O_4$ electrode, suggesting the larger areal capacitance of the hybrid electrodes. The areal capacitances of the three hybrid electrodes increase with the reaction times, which is attributed
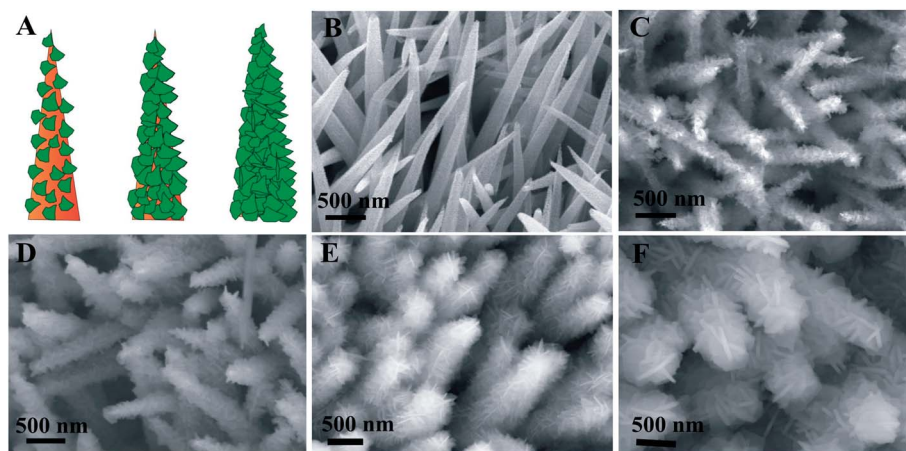

Fig. 4 (A) Schematic illustration of the possible growth mechanism of the $NiCo_2O_4@CoMoO_4$ core/shell nanowire; (B–F) SEM images of the products obtained at different reaction times: (B) 0 h, (C) 4 h, (D) 8 h, (E) 12 h, (F) 18 h.
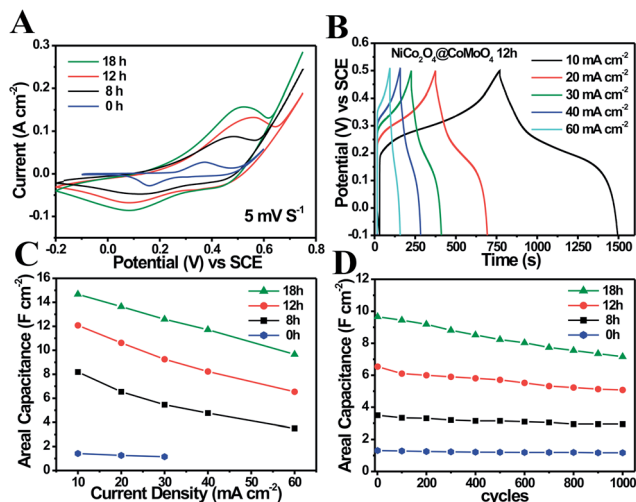
This journal is © The Royal Society of Chemistry 2014

J. Mater. Chem. A, 2014, 2, 4954–4960 | **4957**

Fig. 5 (A) CV curves of the $NiCo_2O_4$ and $NiCo_2O_4@CoMoO_4$ hybrid electrodes recorded at a scan rate of 5 mV s^{-1}; (B) charge–discharge curves of the $NiCo_2O_4@CoMoO_4$ (12 h) hybrid electrode at different current densities; (C) the areal capacitance of the $NiCo_2O_4$ and $NiCo_2O_4@CoMoO_4$ hybrid electrodes as a function of current density plot; (D) cycling performance of the $NiCo_2O_4$ and $NiCo_2O_4@CoMoO_4$ hybrid electrodes.

to the higher mass loading of the shell material ($CoMoO_4$). In the $NiCo_2O_4@CoMoO_4$/Ni foam electrodes, the mass loading of the $NiCo_2O_4$ is about 2.3 mg cm^{-2}, and the mass loading of the $CoMoO_4$ on $NiCo_2O_4$/Ni foam at 8, 12, and 18 h are 4.1, 7.0, and 12.3 mg cm^{-2}, respectively. The mass loading of the $CoMoO_4$ on $NiCo_2O_4$/Ni foam is much higher than that of $CoMoO_4$ directly grown on Ni foam (0.5 mg cm^{-2}).[30]

Galvanostatic charge–discharge tests were further performed in the voltage range of −0.1–0.5 V to estimate the capacitance of the $NiCo_2O_4$ and $NiCo_2O_4@CoMoO_4$ hybrid electrodes. As an example, the galvanostatic charge–discharge curves of the $NiCo_2O_4@CoMoO_4$ (12 h) hybrid electrode at different current densities ranging from 10 to 60 mA cm^{-2} are shown in Fig. 5B. The specific capacitances at various discharge current densities for the three hybrid electrodes are calculated and shown in Fig. 5C. At a current density of 10 mA cm^{-2}, the areal capacitance of the $NiCo_2O_4@CoMoO_4$ (8, 12, and 18 h) hybrid electrodes are 8.19, 12.08, and 14.67 F cm^{-2}, respectively, which are several times larger than the pristine $NiCo_2O_4$ electrode (1.42 F cm^{-2}). This result is encouraging and much higher than those of previously reported core/shell nanostructure array based binder-free electrodes, such as $NiCo_2O_4@MnO_2$ NWAs (2.06 F cm^{-2} at 10 mA cm^{-2}),[27] $Ni_{0.25}Co_{0.75}(OH)_2$ nanowire@nanoplatelet arrays (9.59 F cm^{-2} at 5 mA cm^{-2}).[34] When at a current density of 10 mA cm^{-2}, the specific capacitance of the $NiCo_2O_4@CoMoO_4$ (8, 12, and 18 h) hybrid electrodes are 1280.2, 1347.3, and 1004.7 F g^{-1}, respectively, which are higher than the pristine $NiCo_2O_4$ electrode (616.6 F g^{-1}). From these results, it can be noticed that the greater mass loading of $CoMoO_4$ can lead to higher areal capacitance, but the specific capacitance is decreased. This is because the high mass loading results in increasing thickness of $CoMoO_4$ film on $NiCo_2O_4$/Ni

foam as well as the thickness of $CoMoO_4$ NPs. It is well accepted that pseudocapacitors store charge only in the first few nanometres from the surface.[6,35] Therefore, when the mass loading increases, the electrode material underneath becomes "dead" or "inactive" and cannot participate in the Faradaic reactions, leading to low specific capacitance instead. On increasing the current density, the areal capacitances decrease sharply, indicating the rate capability of the $NiCo_2O_4@CoMoO_4$ hybrid electrodes is not very good. This decrease in area capacitance is because some regions become inaccessible to ions with increasing current density. That is, at a low current density ions have enough time to penetrate into the inner portion of the electrode material. However, only the outer surface of the electrode material can be utilized by ions at higher scan rates.[36,37] Nevertheless, the $NiCo_2O_4@CoMoO_4$ hybrid electrodes (8, 12, and 18 h) still exhibit high capacitances of 3.50, 6.54 and 9.66 F cm^{-2} at a very high current density of 60 mA cm^{-2}. In this work, about 65.8% of the capacitance is retained for the $NiCo_2O_4@CoMoO_4$ hybrid NWAs (18 h) when the discharge current increases from 10 to 60 mA cm^{-2}, which is much better than the $CoO@Ni(OH)_2$ hybrid structure (56.5% of the capacitance retention from 5 to 40 mA cm^{-2}) and the $Ni(OH)_2$ nanowall film (43% of the capacitance retention from 5 to 30 mA cm^{-2}).[38,39] In some cases, for applications such as small scale electronics and stationary energy storage devices, the amount of energy stored per unit area is more important than energy per unit mass.[40] The energy and power densities of the $NiCo_2O_4@CoMoO_4$ hybrid electrodes are also impressive in this work. When at a current density of 10 mA cm^{-2}, the energy densities of the $NiCo_2O_4@CoMoO_4$ (0, 8, 12, and 18 h) hybrid electrodes are 6.0×10^{-5}, 4.1×10^{-4}, 6.0×10^{-4}, and 7.3×10^{-4} W h cm^{-2}, corresponding to 26.1, 64.1, 64.9 and 50.2 W h Kg^{-1}, respectively. The power densities of the $NiCo_2O_4@CoMoO_4$ (0, 8, 12, and 18 h) hybrid electrodes are 1205, 469, 322 and 205 W Kg^{-1}, respectively. These results are higher than the MnO_2–NiO array and $Ni(OH)_2$–MnO_2 core/shell nanostructure electrodes.[40,41]

In addition, the long-term cycle stability of the $NiCo_2O_4@CoMoO_4$ hybrid electrodes was also investigated by repeating the chronopotentiometry (CP) tests at a very high current density of 60 mA cm^{-2} for 1000 cycles, as shown in Fig. 5D. As a comparison, the cycle stability of the pristine $NiCo_2O_4$ electrode at a high current density of 15 mA cm^{-2} is also displayed in Fig. 5D. For $NiCo_2O_4$ electrode, at the discharge current density of 15 mA cm^{-2}, the areal capacitance is about 1.17 F cm^{-2} after 1000 cycles (about 89.3% retention). Impressively, even at a very high discharge current density, the $NiCo_2O_4@CoMoO_4$ hybrid electrodes still exhibit a good long-term electrochemical stability. After 1000 cycles, the areal capacitance of the three $NiCo_2O_4@CoMoO_4$ (8, 12, and 18 h) hybrid electrodes are about 2.95 F cm^{-2} (about 84.3% retention), 5.08 F cm^{-2} (about 77.7% retention), and 7.16 F cm^{-2} (about 74.1% retention), respectively. As an example, the SEM image of the $NiCo_2O_4@CoMoO_4$ (12 h) electrode after 1000 cycles is shown in Fig. 6A. After long-term cycling, the $NiCo_2O_4@CoMoO_4$ (12 h) hybrid nanostructures are well maintained with little structural deformation.

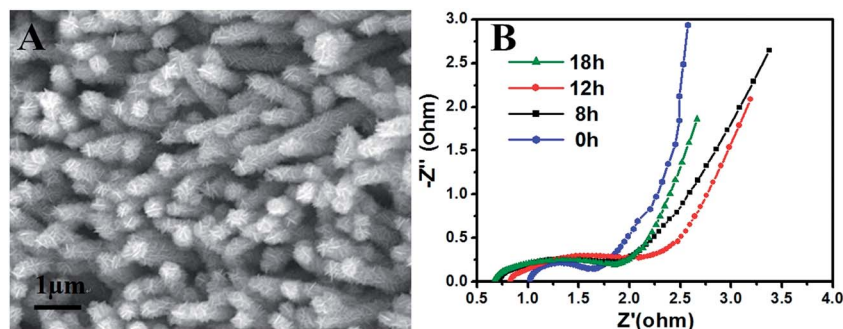4958 | J. Mater. Chem. A, 2014, 2, 4954–4960

This journal is © The Royal Society of Chemistry 2014

Fig. 6 (A) SEM image of the NiCo$_2$O$_4$@CoMoO$_4$ (12 h) hybrid NWAs supported on Ni foam after 1000 cycles; (B) impedance Nyquist plots of the NiCo$_2$O$_4$ and NiCo$_2$O$_4$@CoMoO$_4$ hybrid electrodes.

The electrochemical impedance spectrum (EIS) was further carried out to investigate the electrochemical behavior of the NiCo$_2$O$_4$ and NiCo$_2$O$_4$@CoMoO$_4$ hybrid electrodes. The corresponding Nyquist plots are shown in Fig. 6B. The impedance spectra display a similar form with a semicircle at a higher frequency region and a spike at lower frequency. In the low frequency area, the slope of the curve shows the Warburg resistance (Z_w) which represents the electrolyte diffusion to the electrode surface. Fig. 6B shows that Z_w values are almost the same for the four electrodes. In the high frequency area, the intersection at the real part (Z') indicates the bulk resistance R_s of the electrochemical system, and the semicircle corresponds to the charge transfer resistance R_{ct} caused by the Faradaic reactions and the double-layer capacitance (C_{dl}) on the electrode material surface.[42–44] From the plots, we can see that the NiCo$_2$O$_4$@CoMoO$_4$ hybrid electrodes display lower bulk resistance than the NiCo$_2$O$_4$ electrode. The slight increase of the charge transfer resistance R_{ct} is probably attributed to the low electrical conductivity of the CoMoO$_4$ with respect to the NiCo$_2$O$_4$.[45] Nevertheless, it should be noted that both the bulk resistance and charge transfer resistance of the NiCo$_2$O$_4$@CoMoO$_4$ hybrid electrodes are much lower than that of directly growing CoMoO$_4$ NPs on Ni foam. These results above are responsible for the excellent electrochemical performance of the NiCo$_2$O$_4$@CoMoO$_4$ hybrid nanostructure.

4. Conclusion

In summary, a novel hybrid nanostructure with two binary electroactive materials (NiCo$_2$O$_4$ nanowire and CoMoO$_4$ nanoplate) has been fabricated on a 3D nickel foam *via* a facile two-step hydrothermal method. At a current density of 10 mA cm^{-2}, the areal capacitance of the NiCo$_2$O$_4$@CoMoO$_4$ (8, 12, and 18 h) hybrid electrodes are 8.19, 12.08, and 14.67 F cm^{-2}, respectively, which are several times larger than the pristine NiCo$_2$O$_4$ electrode (1.42 F cm^{-2}). The excellent electrochemical performance indicates that the integration of two promising pseudocapacitive metal oxides into one intriguing core/shell hybrid nanostructure that is directly aligned on the current collector significantly enhances the areal capacitance. This work reveals the importance of rational design and synthesis of smart electrode architectures for high performance SCs. It is believed that

the NiCo$_2$O$_4$@CoMoO$_4$ hybrid electrodes would hold great promise for high-performance supercapacitor applications.

References

1 C. Liu, F. Li, L. P. Ma and H. M. Cheng, *Adv. Mater.*, 2010, **22**, E28–E62.
2 A. S. Arico, P. Bruce, B. Scrosati, J. M. Tarascon and W. V. Schalkwijk, *Nat. Mater.*, 2005, **4**, 366–377.
3 Y. Huang, J. J. Liang and Y. S. Chen, *Small*, 2012, **8**, 1805–1834.
4 Y. M. He, W. J. Chen, X. D. Li, Z. X. Zhang, J. C. Fu, C. H. Zhao and E. Q. Xie, *ACS Nano*, 2013, **7**, 174–182.
5 Y. Wang and Y. Xia, *Adv. Mater.*, 2013, **25**, 5336–5342.
6 P. Simon and Y. Gogotsi, *Nat. Mater.*, 2008, **7**, 845–854.
7 J. Chmiola, G. Yushin, Y. Gogotsi, C. Portet, P. Simon and P. L. Taberna, *Science*, 2006, **313**, 1760–1763.
8 X. Xiao, X. Peng, H. Jin, T. Li, C. Zhang, B. Gao, B. Hu, K. Huo and J. Zhou, *Adv. Mater.*, 2013, **25**, 5091–5097.
9 X. Tao, J. Du, Y. Sun, S. Zhou, Y. Xia, H. Huang, Y. Gan, W. Zhang and X. Li, *Adv. Funct. Mater.*, 2013, **23**, 4745–4751.
10 L. L. Zhang and X. S. Zhao, *Chem. Soc. Rev.*, 2009, **38**, 2520–2531.
11 G. Wang, L. Zhang and J. Zhang, *Chem. Soc. Rev.*, 2012, **41**, 797–828.
12 W. Wei, X. Cui, W. Chen and D. G. Ivey, *Chem. Soc. Rev.*, 2011, **40**, 1697–1721.
13 G. Q. Zhang, H. B. Wu, H. E. Hoster, M. B. Chan-Park and X. W. Lou, *Energy Environ. Sci.*, 2012, **5**, 9453–9456.
14 S. Chen, W. Xing, J. Duan, X. Hu and S. Z. Qiao, *J. Mater. Chem. A*, 2013, **1**, 2941–2954.
15 J. Duay, E. Gillette, J. Hu and S. B. Lee, *Phys. Chem. Chem. Phys.*, 2013, **15**, 7976–7993.
16 C. Yuan, L. Yang, L. Hou, L. Shen, X. Zhang and X. W. Lou, *Energy Environ. Sci.*, 2012, **5**, 7883–7887.

This journal is © The Royal Society of Chemistry 2014

J. Mater. Chem. A, 2014, **2**, 4954–4960 | **4959**

17 C. Yuan, L. Yang, L. Hou, J. Li, Y. Sun, X. Zhang, L. Shen, X. Lu, S. Xiong and X. W. Lou, *Adv. Funct. Mater.*, 2012, **22**, 2560–2566.

18 C. Yuan, J. Li, L. Hou, X. Zhang, L. Shen and X. W. Lou, *Adv. Funct. Mater.*, 2012, **22**, 4592–4597.

19 J. Jiang, Y. Y. Li, J. P. Liu and X. T. Huang, *Nanoscale*, 2011, **3**, 45–58.

20 Y. Li, B. Tan and Y. Wu, *Nano Lett.*, 2008, **8**, 265–270.

21 C. C. Hu, K. H. Chang, M. C. Lin and Y. T. Wu, *Nano Lett.*, 2006, **6**, 2690–2695.

22 J. Jiang, Y. Li, J. Liu, X. Huang, C. Yuan and X. W. Lou, *Adv. Mater.*, 2012, **24**, 5166–5180.

23 G. Zhang, T. Wang, X. Yu, H. Zhang, H. Duan and B. Lu, *Nano Energy*, 2013, **2**, 586–594.

24 X. H. Xia, J. P. Tu, Y. Q. Zhang, X. L. Wang, C. D. Gu, X. B. Zhao and H. J. Fan, *ACS Nano*, 2012, **6**, 5531–5538.

25 W. J. Zhou, X. H. Cao, Z. Y. Zeng, W. H. Shi, Y. Y. Zhu, Q. Y. Yan, H. Liu, J. Y. Wang and H. Zhang, *Energy Environ. Sci.*, 2013, **6**, 2216–2221.

26 J. P. Liu, J. Jiang, C. W. Cheng, H. X. Li, J. X. Zhang, H. Gong and H. J. Fan, *Adv. Mater.*, 2011, **23**, 2076–2081.

27 L. Yu, G. Q. Zhang, C. Z. Yuan and X. W. Lou, *Chem. Commun.*, 2013, **49**, 137–139.

28 Q. Li, Z. L. Wang, G. R. Li, R. Guo, L. X. Ding and Y. X. Tong, *Nano Lett.*, 2012, **12**, 3803–3807.

29 X. Y. Liu, Y. Q. Zhang, X. H. Xia, S. J. Shi, Y. Lu, X. L. Wang, C. D. Gu and J. P. Tu, *J. Power Sources*, 2013, **239**, 157–163.

30 D. Guo, H. Zhang, X. Yu, M. Zhang, P. Zhang, Q. Li and T. Wang, *J. Mater. Chem. A*, 2013, **1**, 7247–7254.

31 Q. Wang, X. Wang, B. Liu, G. Yu, X. Hou, D. Chen and G. Shen, *J. Mater. Chem. A*, 2013, **1**, 2468–2473.

32 M. C. Liu, L. B. Kong, C. Lu, X. J. Ma, X. M. Li, Y. C. Luo and L. Kang, *J. Mater. Chem. A*, 2013, **1**, 1380–1387.

33 J. Zhao, Q. S. Wu and M. Wen, *J. Mater. Sci.*, 2009, **44**, 6356–6362.

34 W. Zhu, Z. Lu, G. Zhang, X. Lei, Z. Chang, J. Liu and X. Sun, *J. Mater. Chem. A*, 2013, **1**, 8327–8331.

35 J. Wang, J. Polleux, J. Lim and B. Dunn, *J. Phys. Chem. C*, 2007, **111**, 14925–14931.

36 C. Mondal, M. Ganguly, P. K. Manna, S. M. Yusuf and T. Pal, *Langmuir*, 2013, **29**, 9179–9187.

37 D. Sarkar, G. G. Khan, A. K. Singh and K. Mandal, *J. Phys. Chem. C*, 2013, **117**, 15523–15531.

38 C. Guan, X. Li, Z. Wang, X. Cao, C. Soci, H. Zhang and H. J. Fan, *Adv. Mater.*, 2012, **24**, 4186–4190.

39 Z. Lu, Z. Chang, W. Zhu and X. Sun, *Chem. Commun.*, 2011, **47**, 9651–9653.

40 J. Liu, J. Jiang, M. Bosman and H. J. Fan, *J. Mater. Chem.*, 2012, **22**, 2419–2426.

41 H. Jiang, C. Li, T. Sun and J. Ma, *Chem. Commun.*, 2012, **48**, 2606–2608.

42 C. W. Huang and H. S. Teng, *J. Electrochem. Soc.*, 2008, **155**, A739–A744.

43 Z. Fan, J. Yan, T. Wei, L. Zhi, G. Ning, T. Li and F. Wei, *Adv. Funct. Mater.*, 2011, **21**, 2366–2375.

44 C. Guan, J. P. Liu, C. W. Cheng, H. X. Li, X. L. Li, W. W. Zhou, H. Zhang and H. J. Fan, *Energy Environ. Sci.*, 2011, **4**, 4496–4499.

45 X. Xia, Z. Zeng, X. Li, Y. Zhang, J. Tu, N. C. Fan, H. Zhang and H. J. Fan, *Nanoscale*, 2013, **5**, 6040–6047.